Swimming upstream: self-propelled nanodimer motors in a flow†

Yu-Guo Tao* and Raymond Kapral*

Received 11th September 2009, Accepted 13th November 2009
First published as an Advance Article on the web 22nd December 2009
DOI: 10.1039/b918906h

The dynamics of chemically-powered self-propelled nanodimer motors in a fluid flow are investigated. The dimer motors are confined to move in a square channel within which a Poiseuille-like fluid flow exists. The flow direction is opposite to that of the nanomotor's directed motion. Simulations of the dynamics are carried out using mesoscopic hybrid molecular dynamics/multiparticle collision dynamics. The simulations of the Poiseuille flow in a square channel are in accord with analytical results for this type of flow. The upstream swimming of the nanodimers is studied as a function of the fluid flow velocity, channel width and interaction strength with the walls and fluid particles. The channel width determines the flow behavior in the channel, while the interaction potentials between the noncatalytic monomer and solvent molecules control the self-propulsion velocity of the nanodimer.

1 Introduction

Molecular motors that convert chemical energy into directed motion along filament substrates are widespread in nature.[1–3] Most self-propelled movement in the cell is carried out by biological machines[4] where chemical species, such as adenosine triphosphate (ATP), are utilized as fuel to induce conformational transitions that give rise to the directed motion. In particular, cytoplasmic motors, such as myosins, dyneins and kinesins play essential roles in cellular transport and, therefore, have been studied extensively both experimentally and theoretically.[5–9] These motors usually operate in a fluid environment in the low Reynolds number regime.[10,11]

In addition to biological machines, artificial synthetic nano- or micron-scale motors have attracted considerable theoretical and experimental interest.[12–14] Such synthetic motors include model swimmers driven by non-reciprocal conformational changes[15–25] and motors without moving parts driven by chemical reactions.[26–41] A number of different mechanisms have been suggested to describe the self-propelled motion of these molecular motors including electro-kinetic pumping,[32] interfacial tension gradients,[27] diffusiophoretic driving[38] and gravitational forces.[35]

While the potential applications of synthetic nanomotors are still being explored, some of the possible applications for these small machines include acting as vehicles for drug delivery and other cargo transport, active chemical synthesis and targeted pollution control. The design of synthetic self-propelled nanomotors with specified directed motion constitutes an increasingly important area of research in nanotechnology. In many such possible applications the molecular motor must be able to function in a flowing fluid environment. This is the case for drug delivery and also for applications involving microfluidic devices where suitably fabricated nanomotors could be used to alter flow properties of the device or carry out synthetic tasks. Consequently, it is of interest to study how molecular motors move in a fluid flow and to investigate the factors that control their motion. In this paper we examine these issues for a nanodimer motor, a simple example of a chemically powered motor.[39–41]

The nanodimer motor consists a pair of catalytic and chemically inactive monomer spheres separated by a fixed internuclear separation. Our simulations of this motor are carried out using a mesoscopic hybrid simulation algorithm.[42–44] The nanodimer directed motion can be controlled by adjusting the monomer sizes, dimer internuclear separation, chemical reaction rates, solvent viscosity, and the nature of the interactions between the noncatalytic sphere and solvent molecules. The effect of an applied external force on the nanodimer dynamics has been investigated and its efficiency has been computed.[41] Recently, the dynamics of a sphere dimer, comprising a non-catalytic silica sphere connected to a catalytic platinum sphere, has been fabricated and studied experimentally.[45]

The outline of the paper is as follows. In Section 2 we briefly describe the particle-based mesoscopic model for the dimer and solvent. Section 3 considers the fluid dynamics. In the absence of a nanodimer motor, the solvent velocity profiles are simulated and compared with theoretical predictions for both slip and stick boundary conditions. An analysis of the principal factors which control the self-propulsion of the nanodimer motor in the flow are discussed in Section 4. Simulation results are analyzed in terms of a microscopic propulsion mechanism. Finally, the conclusions of the study are given in Section 5.

2 Model system

The system we investigate is a nanodimer motor confined to a channel with a square cross-sectional area in which a fluid flow exists. The chemically-powered nanodimer is as same as that studied earlier.[39–41] It comprises catalytic (C) and noncatalytic (N) spherical monomers linked by a rigid bond of length R. The chemical reaction, $A + C \rightleftharpoons B + C$, occurs at the catalytic sphere with probability p_f whenever A encounters the C monomer.[46] Here the reverse reaction probability is taken $p_r = 1 - p_f$,

Chemical Physics Theory Group, Department of Chemistry, University of Toronto, Ontario, Canada M5S 3H6. E-mail: ytao@chem.utoronto.ca; rkapral@chem.utoronto.ca

† This paper is part of a *Soft Matter* themed issue on Emerging Themes in Soft Matter: Responsive and Active Soft Materials. Guest Editors: Anna C. Balazs and Julia Yeomans.

although this probability can be chosen independently of p_f. The dimer motor moves in a square channel containing A and B molecules. The channel is formed by two sets of parallel walls in the x and y directions, separated by a distance L. Each monomer in the dimer interacts with the solid walls through a $9-3$ Lennard-Jones (LJ) potential, $V_{LJ}^{93}(r) = \varepsilon_w[(\sigma_w/r)^9 - (\sigma_w/r)^3]$, where ε_w and σ_w are the wall potential and distance parameters, respectively. We take $\sigma_w = 0.5L$. This potential restricts the dimer motion to occur largely along z, although motion in the x and y directions is not excluded. The relative importance of directed motion along the dimer axis and rotational Brownian motion depends on the size of the nanodimer and magnitude of the propulsive force. In the absence of a confining potential the dimer translates many times its body length before reorientation for the system parameters employed in this study.[39–41] Without a confining potential, in addition to effects due to rotational Brownian motion, reorientation of the dimer by the velocity gradient of the fluid flow can also occur. Our narrow confining channels suppress such reorientation effects making the analysis simpler. Such confinement in narrow channels is appropriate in some physical situations but the study of flow effects on the reorientation of self-propelled objects is an interesting topic to study.

The solvent molecules are modeled by a large number of (typically 10^6) point-like A and B particles with identical masses, m, and continuous positions and velocities. The masses of the catalytic and noncatalytic spheres are adjusted according to their diameters, d_C and d_N, to ensure that the dimer has approximately the same mass density as the solvent. The A molecules interact with both monomers through repulsive LJ potentials, $V_{LJ}^{R}(r) = 4\varepsilon_A[(\sigma_S/r)^{12} - (\sigma_S/r)^6 + 1/4]$, $r \le r_c$, where $r_c = 2^{1/6}\sigma_S$ is the cutoff distance and S = C, N. The solvent B molecules interact with the catalytic sphere through the same repulsive LJ potentials, but interact with the noncatalytic sphere through either repulsive LJ potentials with different energy parameters ε_B, or truncated attractive LJ potentials, $V_{LJ}^{A}(r) = 4\varepsilon_B[(\sigma_N/r)^{12} - (\sigma_N/r)^6]\ s(r)$, where $s(r)$ is a switching function to smoothly truncate the potential to zero.

The dynamics is simulated by a hybrid particle-based mesoscopic molecular dynamics (MD)/multiparticle collision dynamics (MPC) algorithm that consists of streaming and collision steps.[42,43] In the streaming step, the dynamics of both the solvent molecules and dimer monomers are governed by Newton's equation of motion. Note that there are no solvent–solvent forces in this step of the dynamics. In the collision step, solvent molecules are sorted into cubic cells with lattice size a_0. Multi-particle collisions are performed independently in each cell, and the postcollision velocity of particle i in cell ξ is given by $\mathbf{v}'_i = \mathbf{V}_\xi + \hat{\omega}_\xi(v_i - \mathbf{V}_\xi)$, where $\hat{\omega}_\xi$ is a rotation matrix and $\mathbf{V}_\xi$ is the center-of-mass velocity of that cell. In order to insure that Galilean invariance is satisfied for systems with small mean free path λ, random grid shifts are applied in each direction of the simulation box. This method is microcanonical, satisfies mass, momentum and energy conservation, and also preserves phase space volumes. Furthermore, hydrodynamic interactions, which are important for the nanomotor dynamics, are properly taken into account. Technical details of the implementation of this method and examples of its applications are given in recent reviews[47,48] and references therein.

A constant external force field is applied to the solvent molecules along the z direction to induce solvent flow in the channel. Periodic boundary conditions are applied along the z direction, while solvent molecules collide with the solid walls either through collisions in which their velocities change sign, except for the component along the flow direction, to produce slip boundary conditions, or through bounce-back collisions to produce no-slip boundary conditions. The system is subdivided into L_z/a_0 cells in the z direction, but $L/a_0 + 1$ cells in both the x and y directions due to the existence of random grid shifts.[49,50] At the walls, some cells are not completely filled by particles. In this case, extra virtual point particles, whose velocities are drawn from a Maxwell–Boltzmann distribution with zero mean velocity and variance $\sqrt{k_B T/m}$, are added to conserve the solvent particle number density. Moreover, due to the existence of the external force field, a thermostat is used to keep the system temperature constant.[51] More specifically, the simulation box is subdivided into L^2/a_0 strips parallel to both walls. In each strip, the new velocity $\mathbf{v}'_i$ of each solvent particle i in cell ξ is obtained by rescaling the velocity relative to the center-of-mass velocity of that cell, $\mathbf{v}'_i = \mathbf{V}_\xi + \sqrt{\frac{k_B T}{k_B T'}}(\mathbf{v}_i - \mathbf{V}_\xi)$, where $k_B T'$ is calculated from the actual velocity distribution: $\sum_{I \in Strip} \sum_{i=1}^{N_I} \frac{1}{2} m(\mathbf{v}_i - \mathbf{V}_{\xi,I})^2 = (\sum_{I \in Strip} N_I - \tilde{N}) k_B T'$, where N and $\tilde{N}$ denote the number of particles in cell I and the number of cells which contain particles within the specified strip, respectively.

In order to mimic the fluxes of reactive species into and out of the system that drive it out of equilibrium and lead to the establishment of a nonequilibrium steady state, B molecules are converted back to A molecules when they diffuse far enough away from the catalytic monomer. In our simulations, all quantities are reported in dimensionless LJ units based on energy ε, mass m and distance σ parameters: $r/\sigma \to r$, $t(\varepsilon/m\sigma^2)^{1/2} \to t$ and $k_B T/\varepsilon \to T$. The rotation angle is fixed at $\alpha = 90°$. We chose an average number of particles per cell $\gamma \approx 10$ in all simulations. The masses of both A and B species are taken to be $m = 1$. The MD time step used to integrate Newton's equations of motion with the velocity Verlet algorithm is $\Delta t = 0.01$, while the multiparticle collision time is $\tau = 0.5$. The lattice size of the MPC cell $a_0 = 1$, and the system temperature is kept at $T = 1/6$. The LJ potential parameters are chosen to be $\varepsilon_A = 1.0$ and $\varepsilon_B = 0.1$. For these potential parameters the nanodimer motor moves with the catalytic monomer as its head. The direction of motion is chosen to be opposite to that of the solvent flow field so that the dimer swims upstream. The wall separations are chosen to be either $L =$ 16 or 32, while the simulation box length along the flow direction is $L_z = 50$. The diameters of the catalytic and the noncatalytic spheres are $d_C = 4.0$ and $d_N = 8.0$, respectively. The nanodimer internuclear separation is fixed at $R = 7.7$ by a holonomic constraint.[52] This value of R insures that there are no discontinuous potential changes when B or A molecules are produced during chemical reactions.

3 Flow in the absence of dimer

The constant external force on each solvent molecule induces a steady-state Poiseuille-like flow in the channel in the z direction.

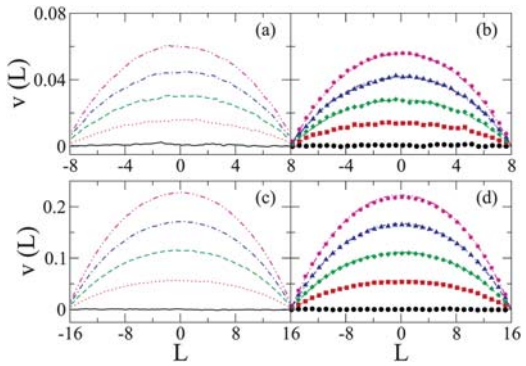

Fig. 1 The solvent velocity profiles when the nanodimer is absent. Results for slip boundary conditions are shown in (a) and (c), and no-slip boundary condition results are shown in (b) and (d). The square channel width is $L = 16$ and 32 for the top and bottom panels, respectively. In each panel, the applied constant external forces on solvent molecules are $F_{ex} = 0$, -1×10^{-4}, -2×10^{-4}, -3×10^{-4} and -4×10^{-4}, respectively, for the plots from bottom to top. The curves through the simulation points, shown in panels (b) and (d), are the theoretical velocity values $v(x, L/2)$ from eqn (1).

Fig. 1 compares the solvent velocity profiles for various values of the strength of the force field for slip and stick boundary conditions. These velocity profiles are taken from narrow slices with unit thickness along the centerline of the channel in the flow direction, parallel to either of the planar walls. Large slips in the velocity profile at the channel walls are observed when slip boundary conditions are applied (see Fig. 1(a) and (c)). These slips increase with an increase in the strength of the external flow and depend on the separation of the channel walls.

With the no-slip boundary condition, the bounce-back rule insures a zero solvent velocity at the channel walls, as shown in Fig. 1(b) and (d). The solvent flow contour profile along the channel is plotted in Fig. 2 for two values of the external force field. The maximum velocity is observed along the centerline of the channel.

The Navier–Stokes equation for Poiseuille flow in a square channel with no-slip boundary conditions at the walls can be written as the Fourier series,

$$v(x,y) = \frac{16}{\pi^4}\frac{F_{ex}}{m}\frac{L^2}{\nu}\sum_{i,j(odd)}^{\infty}\frac{\sin(i\pi x/L)\sin(j\pi y/L)}{ij\left(i^2+j^2\right)} \quad (1)$$

where ν is the kinematic viscosity. At the center of the channel where the velocity is at its maximum we have

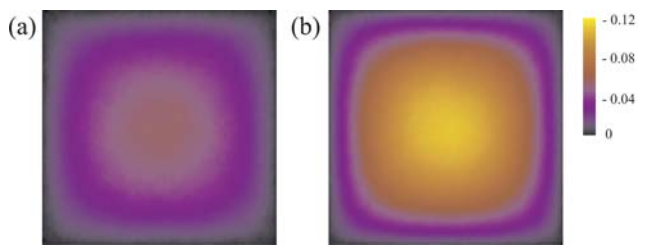

Fig. 2 The solvent velocity profile in the square channel for no-slip boundary conditions for two values of the external force: (a) $F_{ex} = -1 \times 10^{-4}$ and (b) $F_{ex} = -2 \times 10^{-4}$. The channel width is $L = 32$.

$$v_{max} \equiv v(L/2, L/2) = cL^2F_{ex} \quad (2)$$

where the constant,

$$c = \frac{16}{m\nu\pi^4}\sum_{i,j(odd)}^{\infty}\frac{\sin(i\pi/2)\sin(j\pi/2)}{ij\left(i^2+j^2\right)} \approx \frac{16}{m\nu\pi^4}0.448 \quad (3)$$

In the mesoscopic MPC simulations the solvent kinematic viscosity[53–55] is given by

$$\nu = \nu_{kin} + \nu_{col} \quad (4)$$

where ν_{kin} and ν_{col} are the kinetic and collisional contributions to the viscosity whose explicit forms are

$$\begin{aligned}\nu_{kin} &= \frac{k_BT\tau}{a_0^3}\left[\frac{5\gamma}{(\gamma-1+e^{-\gamma})(4-2\cos\alpha-2\cos2\alpha)}-\frac{1}{2}\right],\\ \nu_{col} &= \frac{m(1-\cos\alpha)}{18a_0\tau\gamma}\left(\gamma-1+e^{-\gamma}\right)\end{aligned} \quad (5)$$

Fig. 3 plots the maximum solvent velocity as a function of external force field and compares the simulation results with the theoretical formula in eqn (2). The linear relationship between the maximum solvent velocity and the external force is confirmed. Furthermore, the dashed lines, plotted using eqn (2) with the prefactor c determined from eqn (3) employing the theoretical value of the kinematic viscosity, accurately fit the simulation data points.

Having characterized the flow in the square channel in the absence of a dimer, we next examine how the flow field is modified when a self-propelled dimer is present, and investigate the dimer dynamics in the flow.

4 Dimer dynamics in the flow

In the absence of a flow field we have shown previously[39,40] that the average velocity of the nanodimer along its internuclear axis is $V_z = F_{prop}/\zeta$, where the propulsion force is given by the nonequilibrium average of the total solvent force on the fixed dimer,

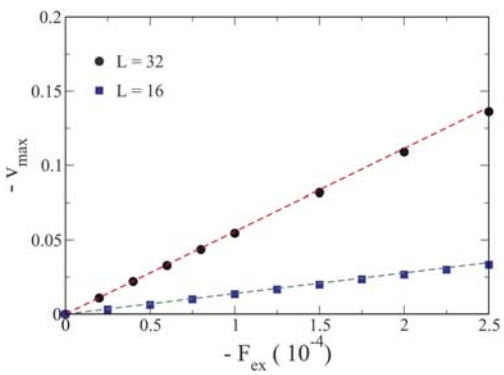

Fig. 3 The maximum solvent velocity as a function of external force. Two square channels with widths of $L = 16$ and 32 are studied. Dashed lines are obtained using eqn (2).

$$F_{\text{prop}} = -\sum_{\alpha=\text{A}}^{\text{B}} \int \mathrm{d}\mathbf{r}\rho_{\alpha}(\mathbf{r})\left(\hat{\mathbf{z}}\cdot\hat{\mathbf{r}}\right)\frac{\mathrm{d}V_{\text{C}\alpha}(r)}{\mathrm{d}r} - \sum_{\alpha=\text{A}}^{\text{B}} \int \mathrm{d}\mathbf{r}\rho_{\alpha}(\mathbf{r})\left(\hat{\mathbf{z}}\cdot\hat{\mathbf{r}}'\right)\frac{\mathrm{d}V_{\text{N}\alpha}(r')}{\mathrm{d}r'} \quad (6)$$

Here $\mathbf{r}$ denotes coordinates measured with the catalytic C sphere as the origin, while $\mathbf{r}'$ is defined with the noncatalytic N sphere as the origin and is related to $\mathbf{r}$ by $\mathbf{r}' = \mathbf{r} - R\hat{\mathbf{z}}$. This formula is easily evaluated once the nonequilibrium steady state density fields $\rho_{\alpha}(\mathbf{r})$ are specified. These may be approximated using the solutions to the diffusion equation with boundary conditions at the catalytic sphere to account for the reversible reaction. The friction coefficient, ζ, can be estimated using the Oseen approximation or directly computed by measuring the average nanodimer velocity when an external force is applied to it.[41]

Next we suppose the nanodimer is immersed in a fluid flow whose direction is opposite to that of the dimer's self-propelled motion. From the results in Fig. 4(a) and (b), if no chemical reaction occurs at the catalytic monomer, the solvent velocity profiles are indistinguishable from those for a flow where no dimer is present. In this case the nanodimer does not execute directed movement in the channel and is advected by the flow. When the chemical reaction A + C → B + C occurs, product B molecules are produced, and a nonequilibrium density gradient is generated in the vicinity of the nanodimer. Along the nanodimer's self-propulsion direction, a solvent "backflow" can be clearly seen at the rear of the noncatalytic monomer (see Fig. 5(a)). Thus, the solvent velocity profiles are depressed in the region around the dimer where chemical reactions take place (indicated by the vertical dashed lines in Fig. 4(c) and (d)). This effect is more evident in systems where the noncatalytic sphere interacts with the B product molecules through stronger attractive forces. As the solvent velocity increases this effect becomes less pronounced since the flow field in the vicinity of the dimer takes the form shown in Fig. 5 (b) near the stall point of the dimer.

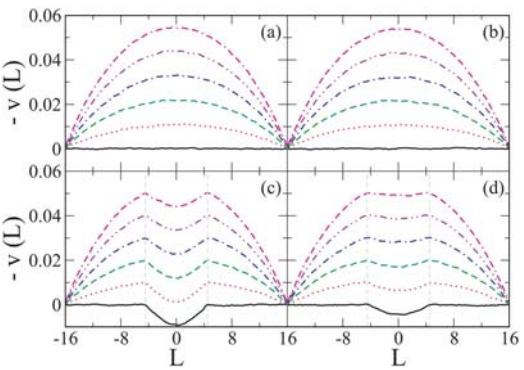

Fig. 4 Solvent velocity profiles. For the results in panel (a), only fluid molecules are contained in the channel, while panels (b), (c) and (d) present results with the nanodimer present. In (b) no chemical reaction occurs at the catalytic sphere so that the system only contains A solvent molecules with a non-reactive dimer. The irreversible chemical reaction A + C → B + C takes place at the catalytic sphere for the results in panels (c) and (d), and the interactions between the noncatalytic monomer and the B solvent molecules are through attractive and repulsive LJ potentials, respectively. The square channel width is $L = 32$ in all simulations. The solvent molecules collide with the walls through bounce-back collisions. In each panel, the applied constant external forces are $F_{\text{ex}} = 0$, -0.2×10^{-4}, -0.4×10^{-4}, -0.6×10^{-4}, -0.8×10^{-4}, and -1.0×10^{-4}, respectively, from bottom to top.

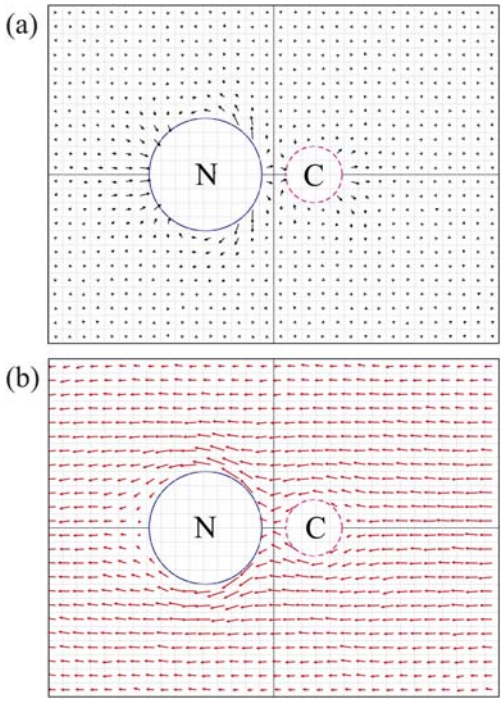

Fig. 5 Solvent molecule velocity field in the vicinity of the dimer spheres. Attractive LJ interactions exist between the noncatalytic sphere and solvent B molecules. The solvent velocity fields are computed from averages in $1 \times 24 \times 32$ slices in the centerline of the channel, parallel to one set of planar walls separated at $L = 32$ along the x direction. The external forces on solvent molecules are $F_{\text{ex}} = 0$ and -1×10^{-4} in (a) and (b), respectively.

In the steady state, the propulsion force is balanced by the frictional force on the dimer in the flow field: $\zeta(V_z - v_{\max}) = F_{\text{prop}}$, where we have approximated the flow field by that at the center of the channel, $v_{\max}$. Using eqn (2), the average steady state velocity of the nanodimer is given by

$$V_z = \frac{1}{\zeta}F_{\text{prop}} + cF_{\text{ex}}L^2 \quad (7)$$

Fig. 6 shows the linear relationship between the average nanodimer velocity V_z and the external force F_{ex} applied on the solvent molecules for various system conditions. (Using a value of 1 mPa·s for the solvent viscosity and a noncatalytic sphere diameter of 1 μm to match that for the real self-propelled dimers which have been fabricated and studied, the dimer velocities are of the order of several μm s^{-1}, in accord with experimental observations.[45]) We have investigated two types of square channel systems where the wall separations are $L = 16$ and 32. The slopes of the lines are approximately four times larger (slope ratio is 4.2) for systems where $L = 32$ than those with $L = 16$, confirming the L^2 dependence in eqn (7). In a narrow channel, the small wall separation may give rise to a change in the value of the frictional force on the nanodimer because of stronger wall–dimer

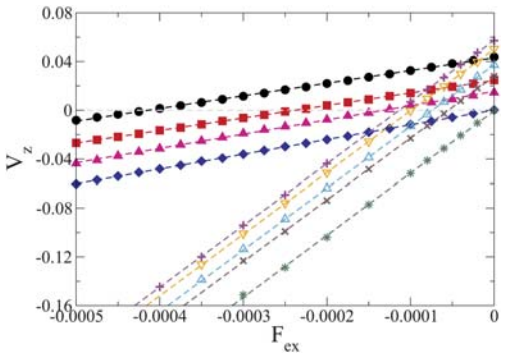

Fig. 6 The average nanodimer velocity V_z as a function of the external force F_{ex} acting on the solvent molecules. For each value of the external force, V_z is an average over 10 independent realizations of the dynamics. Solid symbols are the results for a relatively narrow square channel with width $L = 16$, while the remainder of the results are for systems with $L = 32$. In the simulations shown here, solvent molecules experience bounce-back collisions with the planar walls. Circles, pluses, down-triangles and hollow up-triangles denote results for which interactions between the noncatalytic sphere and B product molecules are through attractive LJ potentials. Squares, solid up-triangles and crosses are used to denote results for repulsive LJ potentials. In this figure we also present results (shown by diamonds and stars) for V_z as a function of F_{ex} when there is no chemical reaction at the catalytic monomer so that only A solvent molecules are present. Two values of the reaction probability are investigated for reversible reactions: $p_f = 0.5$ (up-triangles) and $p_f = 0.8$ (down-triangles).

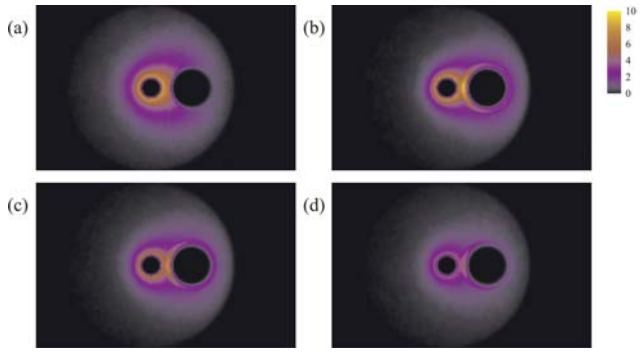

Fig. 7 The average number density profile of B product molecules in the vicinity of the nanodimer taken from slices of $1 \times 32 \times 50$ along the centerline of the channel and parallel to the walls in x direction. The channel width is $L = 32$ in all simulations. In panels (a) and (b), we show results for irreversible chemical reactions, and the interaction potentials between B product molecules and the noncatalytic sphere are either repulsive or attractive. In panels (c) and (d), reversible chemical reactions with probabilities $p_f = 0.8$ and 0.5 occur when A molecules are close enough to the catalytic monomer. In these two simulations B product molecules interact with the noncatalytic sphere through attractive LJ potentials.

interactions. This is likely to be the origin of the small deviation of the slope ratio from four. The nonequilibrium species concentration gradient is an essential element in the propulsion mechanism and, in the absence of fluid flow, diffusion is responsible for the transport of reactive species to the surface of the noncatalytic sphere. For large fluid velocities advection of the reactive species could play a role in this transport. Near the stall point, where the dimer velocity is approximately zero, for our system the average time it takes a solute species to be advected over a distance comparable to the size of the dimer is about the same as the average time it takes to diffuse over the same distance. Since our solute species are mechanically identical, the concentration gradient is along the flow is not affected. Our simulation results show that the advection effect on concentration gradient is not large but this effect should be considered in more detailed theoretical models.

Finally, we briefly discuss how nature the interaction potential (attractive or repulsive) between the noncatalytic monomer and B product molecules, and the type of chemical reaction (irreversible, reversible or no reaction), influences the value of V_z. The reaction rates affect the nonequilibrium density gradient of product molecules that the dimer generates, while the interaction potentials, in conjunction with the chemical gradient, is responsible for the self-propelled motion. These chemical gradients can be seen in Fig. 7 where the average number density profiles of B product molecules are plotted in the absence of an external flow field. As can be seen from the intersections of the linear fits in Fig. 6, the propulsion forces on the nanodimer vary greatly depending on the forms of the chemical reactions and interaction potentials. However, a comparison of the slopes of each line indicates that these factors only induce very small changes in solvent properties, such as local density and viscosity. It is then clear that the relative nanodimer velocity in a square channel depends on several important elements: the channel width, and the nature of the reaction type and interaction potential. The channel width plays a major role in determining the flow behavior, while the chemical reaction and potential controls the nanodimer self-propulsion.

5 Conclusion

Many applications of synthetic nanomotors will likely involve their motion in confined spaces, such as capillaries or microchannels in lab-on-a-chip devices, under conditions where a fluid flow exists. The investigations described in this paper show how such motion depends on characteristics of the channel in which the motion takes place; *e.g.*, the channel width and the nature of the solvent–wall and nanomotor–wall interactions. These factors affect the properties of the flow and the frictional forces that the nanodimer experiences. For the channel and nanodimer dimensions considered here, the product density field that results from the reaction at the catalytic sphere is not strongly influenced by the presence of the confining walls. For smaller channel widths this is not the case and perturbations of this density field can change the concentration gradient in the vicinity of the noncatalytic sphere which, in turn, changes the self-propulsion velocity. Thus, both geometrical and kinetic factors play roles in determining the nanomotor velocity in the channel flow.

Just as an external force with sufficient strength applied to the nanodimer in a direction opposite to its propagation velocity can arrest its motion (stall force), a fluid flow that opposes it motion can also lead to no net nanodimer motion at the stall velocity. We have shown how the nanodimer velocity depends on the fluid flow velocity as well as other dimer and system characteristics. This nanodimer model can be easily extended to a polymer chain

model[56] so that one can consider flexible polymeric motors swimming in a flow. This information should aid in the design of synthetic nanomotors for specific applications.

Acknowledgements

Research supported in part by a grant from the Natural Sciences and Engineering Research Council of Canada.

References

1 R. Ballardini, V. Balzani, A. Credi, M. T. Gandolfi and M. Venturi, *Acc. Chem. Res.*, 2001, **34**, 445–455.
2 V. Balzani, A. Credi and M. Venturi, *Molecular Devices and Machines – A Journey into the Nano World*, Wiley-VCH, Weinheim, 2002.
3 K. Kinbara and T. Aida, *Chem. Rev.*, 2005, **105**, 1377–1400.
4 M. Schliwa and G. Woehlke, *Nature*, 2003, **422**, 759–765.
5 R. D. Vale and R. A. Milligan, *Science*, 2000, **288**, 88–95.
6 N. J. Carter and R. A. Cross, *Nature*, 2005, **435**, 308–312.
7 C. Mavroidis, A. Dubey and M. L. Yarmush, *Annu. Rev. Biomed. Eng.*, 2004, **6**, 363–395.
8 K. Shiroguchi and K. Kinosita Jr, *Science*, 2007, **316**, 1208–1212.
9 A. B. Kolomeisky and M. E. Fisher, *Annu. Rev. Phys. Chem.*, 2007, **58**, 675–695.
10 J. Happel and H. Brenner, *Low Reynolds Number Hydrodynamics*, Nijhoff, Dordrecht, 1965.
11 E. M. Purcell, *Am. J. Phys.*, 1977, **45**, 3–11.
12 G. S. Kottas, L. I. Clarke, D. Horinek and J. Michl, *Chem. Rev.*, 2005, **105**, 1281–1376.
13 Y. Shirai, J.-F. Morin, T. Sasaki, J. M. Guerrero and J. M. Tour, *Chem. Soc. Rev.*, 2006, **35**, 1043–1055.
14 E. R. Kay, D. A. Leigh and F. Zerbetto, *Angew. Chem., Int. Ed.*, 2007, **46**, 72–191.
15 R. Dreyfus, J. Baudry, M. L. Roper, M. Fermigier, H. A. Stone and J. Bibette, *Nature*, 2005, **437**, 862–865.
16 A. Najafi and R. Golestanian, *Phys. Rev. E: Stat., Nonlinear, Soft Matter Phys.*, 2004, **69**, 062901.
17 A. Najafi and R. Golestanian, *J. Phys.: Condens. Matter*, 2005, **17**, S1203–S1208.
18 D. J. Earl, C. M. Pooley, J. F. Ryder, I. Bredberg and J. M. Yeomans, *J. Chem. Phys.*, 2007, **126**, 064703.
19 C. M. Pooley, G. P. Alexander and J. M. Yeomans, *Phys. Rev. Lett.*, 2007, **99**, 228103.
20 D. C. Rapaport, *Phys. Rev. Lett.*, 2007, **99**, 238101.
21 J. R. Howse, R. A. L. Jones, A. J. Ryan, T. Gough, R. Vafabakhsh and R. Golestanian, *Phys. Rev. Lett.*, 2007, **99**, 048102.
22 G. P. Alexander, C. M. Pooley and J. M. Yeomans, *Phys. Rev. E: Stat., Nonlinear, Soft Matter Phys.*, 2008, **78**, 045302.
23 R. Golestanian and A. Ajdari, *Phys. Rev. Lett.*, 2008, **100**, 038101.
24 G. P. Alexander, C. M. Pooley and J. M. Yeomans, *J. Phys.: Condens. Matter*, 2009, **21**, 204108.
25 R. Golestanian and A. Ajdari, *J. Phys.: Condens. Matter*, 2009, **21**, 204104.
26 R. F. Ismagilov, A. Schwartz, N. Bowden and G. M. Whitesides, *Angew. Chem., Int. Ed.*, 2002, **41**, 652–654.
27 W. F. Paxton, K. C. Kistler, C. C. Olmeda, A. Sen, S. K. St. Angelo, Y. Cao, T. E. Mallouk, P. E. Lammert and V. H. Crespi, *J. Am. Chem. Soc.*, 2004, **126**, 13424–13431.
28 S. Fournier-Bidoz, A. C. Arsenault, I. Manners and G. A. Ozin, *Chem. Commun.*, 2005, 441–443.
29 W. F. Paxton, A. Sen and T. E. Mallouk, *Chem.–Eur. J.*, 2005, **11**, 6462–6470.
30 G. A. Ozin, I. Manners, S. Fournier-Bidoz and A. C. Arsenault, *Adv. Mater.*, 2005, **17**, 3011–3018.
31 T. R. Kline, W. F. Paxton, T. E. Mallouk and A. Sen, *Angew. Chem., Int. Ed.*, 2005, **44**, 744–746.
32 Y. Wang, R. M. Hernandez, D. J. Bartlett, J. M. Bingham, T. R. Kline, A. Sen and T. E. Mallouk, *Langmuir*, 2006, **22**, 10451–10456.
33 P. Dhar, T. M. Fischer, Y. Wang, T. E. Mallouk, W. F. Paxton and A. Sen, *Nano Lett.*, 2006, **6**, 66–72.
34 L. Qin, M. J. Banholzer, X. Xu, L. Huang and C. A. Mirkin, *J. Am. Chem. Soc.*, 2007, **129**, 14870–14871.
35 N. I. Kovtyukhova, *J. Phys. Chem. C*, 2008, **112**, 6049–6056.
36 Y. Wang, S.-T. Fei, Y.-M. Byun, P. E. Lammert, V. H. Crespi, A. Sen and T. E. Mallouk, *J. Am. Chem. Soc.*, 2009, **131**, 9926–9927.
37 T. E. Mallouk and A. Sen, *Scientific American*, 2009, **300**, 72–77.
38 R. Golestanian, T. B. Liverpool and A. Ajdari, *Phys. Rev. Lett.*, 2005, **94**, 220801.
39 G. Rückner and R. Kapral, *Phys. Rev. Lett.*, 2007, **98**, 150603.
40 Y.-G. Tao and R. Kapral, *J. Chem. Phys.*, 2008, **128**, 164518.
41 Y.-G. Tao and R. Kapral, *J. Chem. Phys.*, 2009, **131**, 024113.
42 A. Malevanets and R. Kapral, *J. Chem. Phys.*, 1999, **110**, 8605–8613.
43 A. Malevanets and R. Kapral, *J. Chem. Phys.*, 2000, **112**, 7260–7269.
44 A. Malevanets and R. Kapral, *Lect. Notes Phys.*, 2004, **640**, 116–149.
45 L. F. Valadares, Y.-G. Tao, N. S. Zacharia, V. Kitaev, F. Galembeck, R. Kapral and G. A. Ozin, *Small*, 2009, DOI: 10.1002/smll.200901976.
46 K. Tucci and R. Kapral, *J. Chem. Phys.*, 2004, **120**, 8262–8270.
47 R. Kapral, *Adv. Chem. Phys.*, 2008, **140**, 89–146.
48 G. Gompper, T. Ihle, D. M. Kroll and R. G. Winkler, *Adv. Polym. Sci.*, 2009, **221**, 1–87.
49 T. Ihle and D. M. Kroll, *Phys. Rev. E: Stat., Nonlinear, Soft Matter Phys.*, 2001, **63**, 020201.
50 T. Ihle and D. M. Kroll, *Phys. Rev. E: Stat., Nonlinear, Soft Matter Phys.*, 2003, **67**, 066705.
51 Y.-G. Tao, I. O. Götze and G. Gompper, *J. Chem. Phys.*, 2008, **128**, 144902.
52 D. Frenkel and B. Smit, *Understanding Molecular Simulation –From Algorithms to Applications*, Academic Press, San Diego, 1996.
53 N. Kikuchi, C. M. Pooley, J. F. Ryder and J. M. Yeomans, *J. Chem. Phys.*, 2003, **119**, 6388–6395.
54 M. Ripoll, R. G. Mussawisade, K. Winkler and G. Gompper, *Phys. Rev. E: Stat., Nonlinear, Soft Matter Phys.*, 2005, **72**, 016701.
55 J. T. Padding and A. A. Louis, *Phys. Rev. E: Stat., Nonlinear, Soft Matter Phys.*, 2006, **74**, 031402.
56 Y.-G. Tao and R. Kapral, *ChemPhysChem*, 2009, **10**, 770–773.